International Journal of Multiphase Flow 36 (2010) 88–91

Contents lists available at ScienceDirect

International Journal of Multiphase Flow

journal homepage: www.elsevier.com/locate/ijmulflow

Brief Communication

Particle velocity and structures in blast waves imaged using particle image velocimetry

Charles M. Jenkins [a,b,*], Yasuyuki Horie [a], Chang-Yu Wu [b]

[a] Air Force Research Laboratory, Munitions Directorate, Eglin AFB, FL 32542, USA
[b] Department of Environmental Engineering Sciences, University of Florida, Gainesville, FL 32611-6450, USA

ARTICLE INFO

Article history:
Received 18 March 2009
Received in revised form 5 August 2009
Accepted 10 August 2009
Available online 26 August 2009

Keywords:
Blast wave particle flow
Heterogeneous explosive
PIV multiphase flow

1. Introduction

Energetic formulations frequently contain various quantities of reactive metallic particles to increase energy content for blast wave enhancement. The initial mass fraction of the metal powder as well as the particle size and morphology all influence the extent to which the particle combustion couples with blast wave propagation (Frost and Zhang, 2006). The initial shock and particle combustion process provides energy resulting in some amount of energy transfer into particle inertia. Inertia transferred to particulates with different sizes and densities within the blast wave has significant effects on particle dynamics and structure formation within the blast wave. As a result, both the particle flow field and blast wave generated by the detonation of a heterogeneous explosive in a free field differ from that of an ideal homogeneous explosive (Frost and Zhang, 2006). Currently, challenges remain related to the development of robust in-situ diagnostics for probing the flow parameters such as particle and gas temperature, pressure, and particle density and velocity within the multiphase fireball (Frost and Zhang, 2006). While multiphase flow in blast waves has been a subject of interest for many researchers, the specifics of heat and energy transfer are not fully understood due in part from the lack of experimental methods capable of measuring particle motion and gas flow without exterior interference. Particle image velocimetry (PIV) is a means of obtaining high resolution images of particle flow. Balakumar and Adrian (2004) demonstrated the ability to image and perform vector analysis on high velocity non-uniform particles imbedded in solid rocket motor materials and for short duration events it has been demonstrated that PIV can be used to image olive oil droplets dispersed by exploding bridge wires (Murphy et al., 2005). However, no study using a PIV system for determining particle velocity and structure has been reported for explosively driven metallic particles.

The research reported in this communication describes the application of PIV to obtain velocity and particle interaction phenomena. Examples of processes occurring within the blast wave that were observed in the images included particle structure formation, particle velocity information, and particle agglomeration.

2. Experimental setup

A PIV system was used in this research with some portions of the optics modified to provide protection from the harsh environment produced during the detonation of a high explosive (H.E.). The system used a 120 mJ pulsed laser (Model YAG120-15, Big Sky Laser, Quantel) that was frequency doubled from 1064 nm to 532 nm. The Nd:YAG twin cavity pulsed system had a pulse width of 12 ns and was capable of a repetition rate of 15 Hz. Additional system equipment included a synchronizer for control of image and laser timing made by TSI Inc. (Model 610035) capable of 1 ns resolution and TSI Inc. software (Insight 3G) installed on a Dell Precision desk top system for laser, camera control and image processing. Band pass filters of $532 + 2/-0$ nm from Andover Inc. (PN 532FS10-50) were used to reduce the filtered light due to luminosity through the camera lens and enhance the particle's image while

* Corresponding author. Address: Air Force Research Laboratory, Munitions Directorate, Eglin AFB, FL 32542, USA. Tel.: +1 850 882 5902; fax: +1 850 882 3540.
E-mail address: jenkins@eglin.af.mil (C.M. Jenkins).

0301-9322/$ - see front matter Published by Elsevier Ltd.
doi:10.1016/j.ijmultiphaseflow.2009.08.004

providing protection of the CCD imaging chip. The imaging system used a Power View Plus 11MP camera from TSI Inc. (Model No. 630062) with a square pixel size of 9 μm and a Nyquist resolution limit of 55 pixels/mm. The camera was fitted with a 105 mm Nikkor lens (Model No. 610044) made by Nikon and set at an *f*-number = 11. The standoff distance from the light sheet to the surface of the outer lens was 83.8 cm (33 in.) making the magnification about 0.1 M.

The test item used a core of organic explosive made from four stacked ½ × ½ in. cylindrical pellets glued together totaling 10.3 g. Their composition includes 98.5% 1,3,5-trinitro-1,3,5-triazine (RDX) and 1.5% Viton, a fluoro elastomer used as a binder to ensure dimensional stability. Polydispersed aluminum powders used in the tests included H-10 and H-95 made by Valimet Inc. from their spherical powder series, these materials had mean volumetric diameters of 15 μm (H-10) and 129 μm (H-95) and were generally log normally distributed. The powders were used to fill the annular space between the wall of the paper tube and the RDX core (Fig. 1) and provided the tracer particles for PIV tracking.

To ensure repeatable results, the charge configuration was maintained and only the metallic powder nominal diameter was changed for each test series. The internal diameter of the paper tube was built to 1.00 ± 0.006 in. by Yazoo Mills Inc. The annular space of 6.35 mm thickness was maintained by using end caps to center the explosive core. All charges were built by the same technician using the same method of construction. X-ray images of the test items (Fig. 1) were conducted on all charges to ensure no defects such as air gaps or miss alignment of the glued pellets were incorporated into the test charges. A serial number was provided for each charge and a record of dimensional and mass attributes was retained.

To ensure good image quality of the aluminum powders within the FOV, the camera lens was pre-focused on dispersed olive oil droplets within the light sheet prior to start of the experiments. This was accomplished with an atomizer, using a Devilbiss heavy duty air compressor (Model No. 8650D) and a DeVilbiss atomizer (Model No. 163) with a Laskin nozzle to produce 1–2 μm diameter particles as individual light-scattering markers (Murphy et al., 2005). The small low velocity oil droplets have good light reflectance and thus provided a sharp bright image for focusing.

Test charges used in the experiment were hung above the light sheet from a test fixture in a position where the axial centerline of each charge was aligned with the projected laser light sheet (Fig. 2). This ensured that particle flow was parallel to the light sheet and perpendicular to the camera. The arrangement provided a particle flow in a downward direction towards the test chamber's floor (Fig. 2.). The vertical placement of the charge was in a position 83.82 cm from the upper right corner of the camera's field of view (FOV). The lower edge of the FOV was about 1 meter from the chamber's floor. A grid panel of dimension 4 ft wide and 8 ft tall with one centimeter blocks was placed behind the charge prior to firing the charge, it stretched from the charge's hanging position though the FOV and down to the chamber's floor. The grid panel was used to map the charge position with relation to the camera's FOV (18.5 × 28.5 cm), allowing the position of any particle image or structure to be correlated to the position of the charge for later analysis. Each test charge position was recorded with a handheld camera and a video image of the FOV position was made with the PIV camera; this set of images also included a spatial calibration standard. The test standard was recorded before the start of each series with the test charge number recorded in both the PIV software and the setup image.

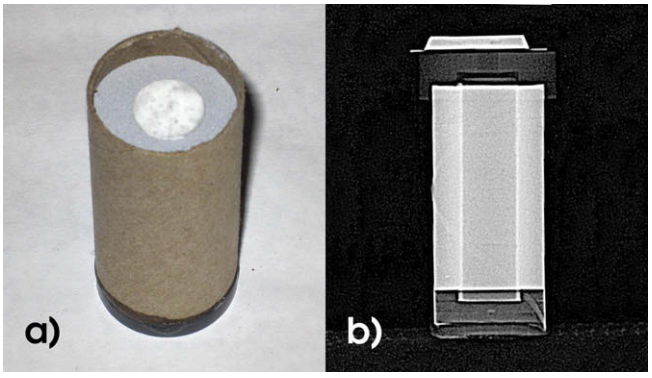

Fig. 1. (a) Annular test charge configuration for powder systems. (b) X-ray of charge to ensure against defects.

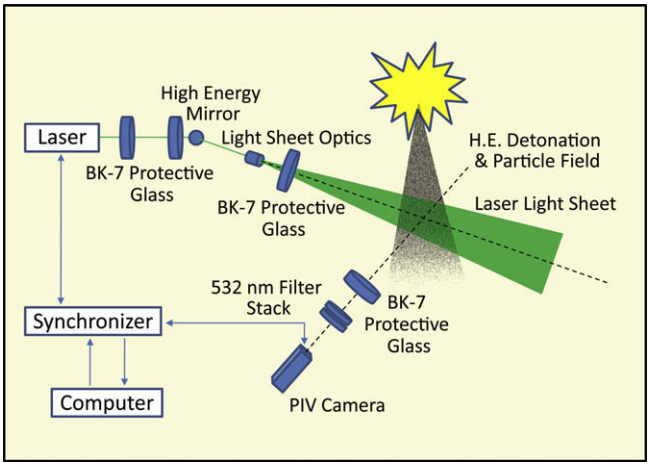

Fig. 2. PIV test setup (top down), high explosive was set above the light sheet with particle flow in a downward direction.

The light sheet distance from the camera's lens was set at 83.82 cm and checked after each test for movement. To ensure particles fell within the PIV camera's FOV, a timing delay for the first image was established at 5.8 ms using the detonator fire pulse from the facility's fire control system. The fire pulse was split and sent to the PIV system software and to the charge's detonator. A difference in cable lengths accounted for only about a 10 ns difference in pulse arrival times (1 ns/m) between software and detonator. The delay time interval between the fire pulse and image A was chosen based on the estimated particle velocity from previous high speed video tests. The Δt value between image A and image B for H-10 powder was 80 μs with a delay time of 5.8 ms and a Δt value for H-95 of 50 μs with a delay time of 5.6 ms. These Δt times were later refined for image displacements of 10–15 pixels in subsequent tests after image analysis had been performed on the first image pairs. The reduction in the time between image frames enhanced the spatial resolution by reducing the size of interrogation regions used in the vector analysis.

3. Results

An example of a raw image can be seen in Fig. 3a. Image preprocessing via background subtraction was used to enhance the particle's image by decreasing the luminescence produced by the H.E. and burning aluminum (Fig. 3b) seen in the images as a light white haze. The analysis process entailed a numerical estimate of background luminosity for each image; this value was subtracted from the entire image. Each image must be processed separately with its own background estimate because of the variances from image to image. The light sheet thickness was set at about 1.0 mm in the camera's FOV; this was check via burn paper during the initial setup for each series of powder sizes. Controlling light sheet thickness can be challenging considering the several protective glass struc-

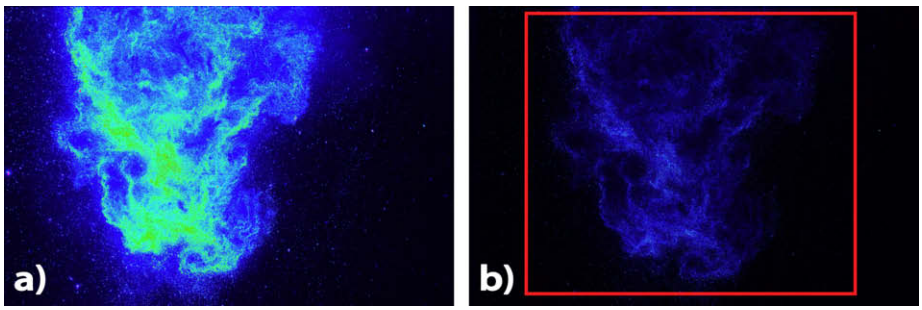

Fig. 3. (a) Raw image of camera's FOV with H-10 aluminum and (b) background subtraction used to reduce luminosity and highlight individual particles for improved vector analysis.

tures, mirror and the gas cloud the beam must pass through before it reaches the camera's FOV.

The proper selection and combination of processing algorithms can significantly influence the analysis product by increasing the number of valid vectors in the flow. The most effective grid engine processor provided in the TSI analysis software for this series of experiments proved to be a Recursive Nyquist Grid Engine and the Hart Correlation approach for the Correlation Engine. The Gaussian Mask was used for the Spot Mask Engine and Gaussian Peak Engine for the Peak Engine while using rectangular interrogation regions. Post-processing used a local validation processor and vector field conditioning setup. A universal median test was used for local validation to remove bad vectors; the universal median is an improved median filter which is a more robust validation method than the mean because the tolerance is less sensitive to the flow field. For vector field conditioning the local median was used for filling holes in the interrogation regions which failed validation. The resulting vector analysis yielded approximately 4500 total vectors in each image, of which about an average of 71.5% were good and the balance interpolated. Most of the bad vectors were associated with the initial analysis from images within the dense structures or those on the inside edge of a structure where the second image comingled within a dense structure. Velocity vector errors and lost images are believed to have primarily fell into three categories (1) images lost from in and out of plane motion (2) images which were lost from high background luminosity or (3) those lost within structures where the structures where so dense that individual particle images could not be determined.

The presences of wave-like structures seen in Fig. 3 were regions determined to be of high particle concentration and velocity while regions of low particle concentration are often associated with lower particle velocities with few velocity vectors supporting the flow. The distribution of these regions can best be seen in the velocity contour plot shown in Fig. 4, where velocities are in meters per second. Velocity contour patterns do not always match exactly with their raw images because of the limitations of PIV at high particle concentration to resolve individual particle images from overlapping images and from losses due to invalid images. Invalid images can be common in this type of flow and lost image pairs can mean a greater number of interpolated vectors are needed to fill holes in otherwise dense particle flow regions. The combination of low velocity, particle voids, a lack of valid image vectors, rotating flow areas, and the shape of the region of interest (ROI, shown boxed in red) selected for analysis can significantly affect the image's statistical values. A very broad range of velocity values were seen over the ROI in most of the processed images for these tests.

Zhang et al. (2001) discusses the ability of very fine particles to equilibrate to the flow of the combustion products whereas larger particles will respond slowly due to their large inertia. Adrian (1991) described the particle lag $|\mathbf{v}-\mathbf{u}|$ resulting from the single

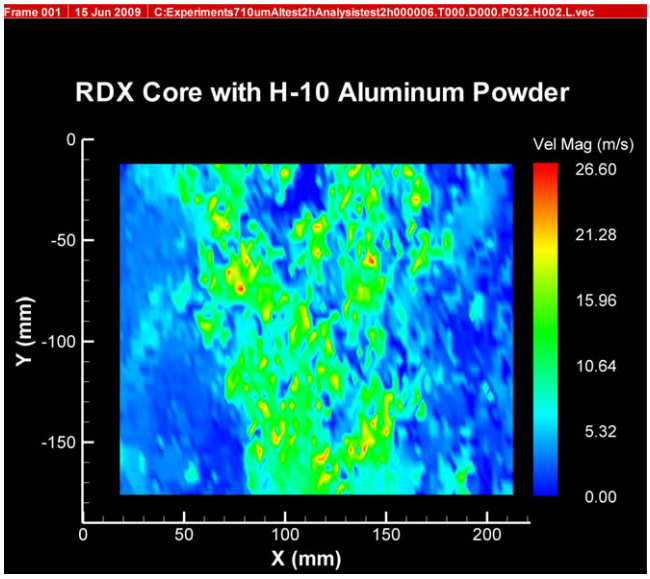

Fig. 4. Velocity contour plot for the particle region outlined for H-10 was cropped for ease of processing. *X* & *Y* dimensions correspond to dimensions of the FOV.

particle slip velocity equation due primarily from the mismatch between fluid and particle density with the larger particle diameters of the same material showing greater velocity separation than the smaller particles. Due to the wide standard deviation (SD) of both of the particle systems, H-10 had a SD = 9.5 μm and the H-95 SD = 34.64 μm, it is likely that this had some influence in the distribution of the particle flow patterns.

$$|\mathbf{v}-\mathbf{u}| = \left|\frac{2}{3}\frac{\rho_p}{\rho}\frac{d_p}{C_D}|\dot{\mathbf{v}}|\right|^{1/2}$$

where $\mathbf{v}$ is the Lagrangian particle velocity, $\mathbf{u}$ is the Eulerian fluid velocity, C_D is the drag coefficient, ρ_p and ρ are the particle and fluid densities and d_p is the particle diameter.

For the larger particle size tested, under the same conditions, significantly less wave-like structures were seen. Greater steepness and luminosity with increased directionality in the particle flow in the *y*-direction was also observed as can be seen in Fig. 5 where background subtraction has not been applied. These observations may be explained in part from the delayed response to acceleration from the shock wave and expanding product gas of the larger H-95 particles.

For H-10, Fig. 4, shows smaller more numerous vector groupings and about 12.0 m/s slower mean velocity than for the H-95 plot in Fig. 6. With the explosive charges kept in the same initial position in Fig. 3 as in Fig. 5, a shift in the ROI position along the *x*-axis, shown boxed, can be seen in the two images. This result

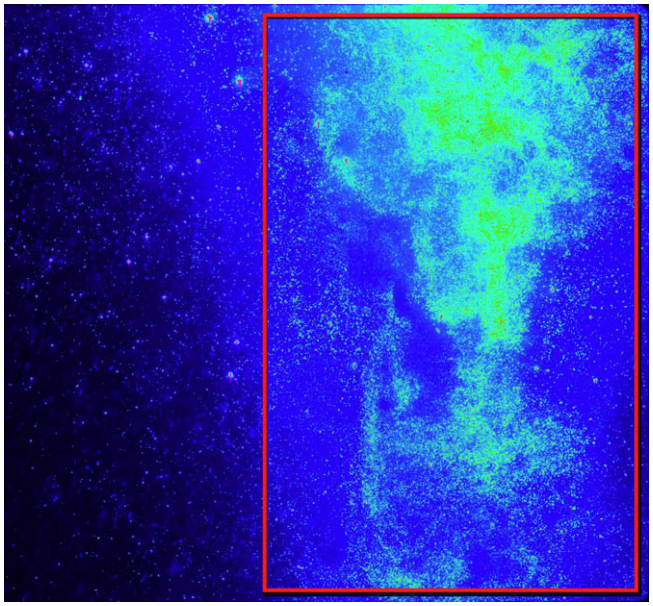

Fig. 5. Raw image of camera's FOV without background subtraction for Valimet H-95 aluminum powder.

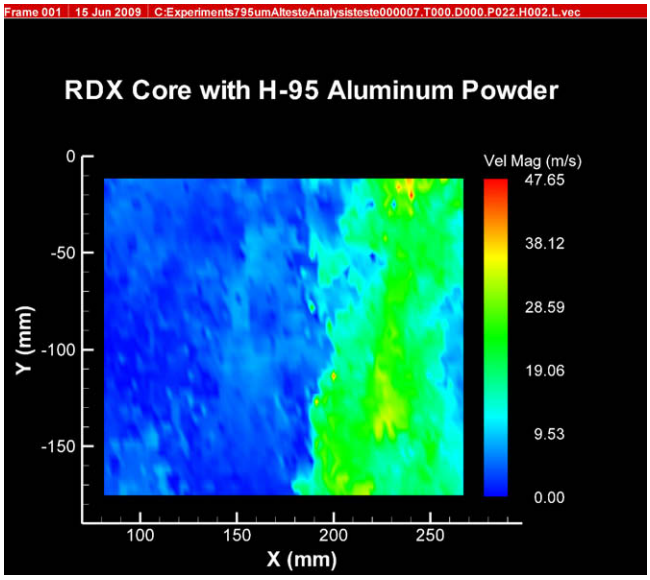

Fig. 6. H-95 powder velocity contour plot for the particle region outlined in Fig. 5.

indicates a smaller *x*-directional component to the left for particles in the contour plots of Fig. 6 than for the particles in Fig. 4 for the H-10 powder.

4. Conclusions

In summary it has been shown that capturing images of particles driven by a high explosive is possible and can provide high quality images resulting in good velocity data. Results from the two different aluminum powder sizes showed that within the blast wave there is a significant difference in particle velocities, structure, resultant particle direction and luminosity. Low vector yield or large numbers of bad vectors can be expected if numerous particle structures exist, particularly, if individual images are not well defined as in a dense structure; in such cases good validation settings are required to remove bad vectors. This may not be a concern for the experimenter if the primary goal of the research is to identify particle phenomena rather than determining fluid velocities in the surrounding gas. Higher velocities in the FOV for H-95 than for H-10 may be related to the inertia properties of the larger particles resisting deceleration as compared to the H-10 of lower mass. The variation in inertia values of the different diameter particles would also explain the greater *x*-axis velocity component or translation along the *x*-axis for H-10. Hot spots, regions of very high velocity in the contour plot are likely the result of miss identified images resulting from high density particle concentrations or irregular shaped particle images, while three sigma variations in velocity are expected to be shown based on existing software settings.

Additional research is continuing with different particle size distributions, charge configurations and material types.

Acknowledgements

This work was sponsored by the US Air Force Research Laboratory at Eglin AFB and the Defense Threat Reduction Agency (DTRA), MIPR # 07-2114 M. Thanks to Dr. Mike Murphy and Dr. Ron Adrian at ASU for clarification on details of their work, Dr. Stamatios Pothos, Dr. Dan Troolin and Dr. Tyson Strand at TSI Incorporated for hands on PIV training and analysis support.

References

Adrian, R.J., 1991. Particle imaging techniques for experimental fluid mechanics. A. Rev. Fluid Mech. 23, 261–268.

Balakumar, B.J., Adrian, R.J., 2004. Particle image velocimetry in the exhaust of small solid rocket motors. Exp. Fluids 36, 166–175.

Frost, D.L., Zhang, F., 2006. The nature of heterogeneous blast explosives. In: Proceedings of the 19th International Symposium on Military Aspects of Blast and Shock. Calgary, AB, Canada.

Murphy, M.J., Adrian, R.J., Stewart, S.D., Elliott, G.S., Thomas, K.A., Kennedy, J.E., 2005. Visualization of blast waves created by exploding bridge wires. J. Visual. 8, 125–135.

Zhang, F., Frost, D.L., Thibault, P.A., Murray, S.B., 2001. Explosive dispersal of solid particles. Shock Waves 10, 431–443.